Microchimica Acta (2021) 188: 299
https://doi.org/10.1007/s00604-021-04958-z

ORIGINAL PAPER

On-off-on fluorescent sensor for glutathione based on bifunctional vanadium oxide quantum dots induced spontaneous formation of MnO_2 nanosheets

Pei Jia[1] · Jinjie Hou[1] · Kairong Yang[1] · Li Wang[1]

Received: 30 May 2021 / Accepted: 25 July 2021 / Published online: 16 August 2021

Abstract

Fluorescence sensing of glutathione by tailor-made chemical sensors is a prospective technique, which could provide simple, fast, and visual detection. Herein, a fluorescence sensor based on vanadium oxide quantum dots (VO_x QDs) and permanganate (MnO_4^-) has been designed for monitoring glutathione. The bifunctional VO_x QDs, possessing rich redox chemistry and robust fluorescence (exhibiting fluorescence near 505 nm upon excitation at 450 nm), were synthesized via cryogenic-mediated liquid-phase exfoliation. In the presence of MnO_4^-, VO_x QDs induced the spontaneous formation of MnO_2 nanosheets which caused the fluorescence quenching. However, the subsequent introduction of glutathione could trigger MnO_2 reduction to Mn^{2+}, and the fluorescence was recovered. Based on this phenomenon, an "on-off-on" fluorescence sensor for glutathione detection was established. Under the optimal conditions, this sensor allowed detection of glutathione in the linear range of 0.5–100 μM with a detection limit of 0.254 μM. Additionally, the proposed strategy revealed the selectivity toward glutathione and the potential of practical application in the analysis of human serum, vegetable, and fruit samples.

Keywords Vanadium oxide quantum dots · Cryogenic exfoliation · Manganese dioxide nanosheets · Fluorescence sensor · Glutathione

Introduction

Glutathione (GSH) is small-molecule that plays pivotal roles in some physiological processes, such as regulating redox balance, maintaining immune system, and transducing intracellular signals [1–4]. It is confirmed that the decreased or elevated levels of GSH in tissue can serve as a caution for many diseases, including liver damage, AIDS, Alzheimer's disease, and cancer [5, 6]. Researchers have proved that dietary supplementation can maintain GSH balance and prevent many undesirable diseases [7]. Particularly, the broad-spectrum detoxification endows GSH with the utility of functional food supplements. Therefore, it is significant to develop reliable and efficient detection strategies for quantification of GSH levels, which could provide the reference for disease diagnosis and daily GSH supplement.

Fluorescence analysis has been considered a promising technique for detecting analytes [8, 9], which becomes a great field of interest to construct sensors [10]. Thereinto, quantum dots (QDs) are a type of nanoparticle with a lateral dimension of less than 10 nm generally. Because size diminution can cause quantum size effects [11], quantum confinements [12], and surface effects [13], they possess lots of superiorities including outstanding fluorescent feature, large surface area, and well dispersion [14, 15]. Vanadium oxides (VO_x) with two-dimensional layered structure have gradually become a rising star in the field of catalysis, lithium batteries, hydrogen storage, anti-bacterials, and so on, which benefit from their prominent properties of obvious redox behavior, electronic transition, and antimicrobial ability [16–18]. Engineering VO_x into quantum dots with intrinsic properties of their bulk forms and unprecedented fluorescence characteristics could endow more potential applications of VO_x while it is still in a nascent stage. Cryogenic-mediated liquid-phase exfoliation is an innovative approach using liquid nitrogen to create ultra-

Pei Jia and Jinjie Hou contributed equally to this work.

✉ Li Wang
lwang@nwsuaf.edu.cn

[1] College of Food Science and Engineering, Northwest A&F University, Yangling 712100, Shaanxi, People's Republic of China

low temperature condition and exfoliate the raw bulk materials into low dimensions [19, 20]. The generation of fragile character and small cracks in the intralayer through cryogenic treatment could facilitate the mechanical splitting and breakdown subsequently [21]. After exposure to room temperature, fractures occurred because of volumetric expansion. Therefore, the cryogenic-mediated liquid-phase exfoliation provides a latent protocol for conversion VO_x into high-quality QDs.

Combination of QDs with fluorescence quenchers has been applied for designing "on-off-on" sensors which is not prone to be interfered by environmental stimulus compared with direct quenching models [22]. Manganese dioxide (MnO_2) nanomaterials are always employed as broad-spectrum quenchers due to the broad and strong optical absorption [23, 24]. Coupling with the unique oxidation ability, many fluorescence switchable platforms were conducted based on the fact that MnO_2 nanostructures can be reduced to Mn^{2+} by reductive species [25]. It is worth noting that the simple synthesis approach of MnO_2 is an essential prerequisite for its extensive applications. Hitherto, with $KMnO_4$ as the Mn source, many bottom-up methods were proposed for preparation of MnO_2 nanomaterials. Sohal et al. synthesized MnO_2 nanospheres through mixing methionine and $KMnO_4$ with continuous stirring for 20 min [26]. Deng et al. exploited 2-(*N*-morpholino)ethanesulfonic acid (MES) as reductant for MnO_2 formation under ultrasonic condition [27]. Although the preparations of MnO_2 were well-documented, the utilization of reducing agents and spending of time casted a shadow over the application in an easier manner. Therefore, it is necessary to look for a simple formation method for MnO_2 nanomaterials.

In this present work, bifunctional VO_x QDs with brilliant fluorescence and redox ability were synthesized via cryogenic-mediated liquid-phase exfoliation and then employed to construct an "on-off-on" fluorescence sensor for glutathione detection. The as-prepared VO_x QDs exhibited blue emission and played a reductive role. After the addition of MnO_4^-, VO_x QDs induced the spontaneous formation of MnO_2 nanosheets, and the fluorescence was quenched as a result of an internal filtration effect (IFE) between VO_x QDs and MnO_2 nanosheets, while the quenched fluorescence of VO_x QDs could be reversed in the presence of GSH which can decompose MnO_2 nanosheets to Mn^{2+}, as illustrated in Scheme 1. Compared with the direct quenching sensor, this switchable sensor was more resistant to environmental stimulus that can improve the analytical performances. Besides, the proposed platform exhibited high selectivity toward GSH than other ions and biomolecules. Moreover, the practicability was successfully validated by detecting GSH in human serum, vegetable, and fruit samples.

Experiments

Synthesis of VO_x quantum dots

VO_x quantum dots were prepared by cryogenic-mediated liquid-phase exfoliation according to the previous literature with some modification [28]. The peeling effects of *N*,*N*-dimethylformamide (DMF), ethanol, and *N*-methylpyrrolidone (NMP) were compared. The details are described in the Supplementary information.

Design of VO_x QDs/MnO_4^- sensor for detecting GSH

Firstly, for the signal-off process, 100 μL of VO_x QDs solution (10 mg/mL) was added to a centrifuge tube and mixed with newly prepared MnO_4^- solution with different final concentrations of 0, 10, 20, 50, 100, 150, 200, 250, 300, 350, and 400 μM. After diluting to 1 mL and vortex for 8 min, the fluorescence spectra were recorded at the excitation wavelength of 330 nm. Thereafter, in the signal-on procedure, GSH was quantified by titration studies. Different volumes of GSH standard solutions were added into the mixture of VO_x QDs/MnO_4^- to keep the final concentrations of 0 to 300 μM and then diluted to 1 mL. Followed by a reaction for 3–4 min, the FL recovery factor ($(F\text{-}F_q)/F_q$) versus the concentration of GSH was used to calculate the regression equation. Moreover, a series of interferers were tested to evaluate the selectivity of the assembled sensor toward GSH, including cations (Na^+, Cu^{2+}, Co^{2+}, Ca^{2+}, Cd^{2+}, Zn^{2+}, K^+, Ba^{2+}, Mg^{2+}, Al^{3+}, Fe^{3+}, Hg^{2+}, Mn^{2+}), anions (Cl^-, CO_3^{2-}, NO_3^-, SO_4^{2-}, Ac^-), amino acids (Ser, Ile, Leu, Val, Pro, Gly, Lys, Asp, Met, Glu, L-Glu, Phe, Arg, Thr, His), and molecules (urea, glucose, BSA, AA, Cys). The concentration of the other interferences (350 μM) were 10 times higher than that of GSH, and AA (105 μM) was three times higher than that of GSH (35 μM).

Optimization of sensing conditions

So as to reach the optimal analytical results for GSH, several experimental conditions that may affect the sensitivity were optimized prior to the application, including the concentration of MnO_4^-, reaction pH and time in the off procedure, and reaction time in the signal-on procedure.

Monitoring GSH in practical samples

Human serum samples were collected from Northwest A&F University hospital (Shaanxi, China). The samples were centrifuged for 10 min at 8000 rpm, and the supernatant was diluted with water for 10^3-fold for further measurement.

The vegetable and fruit samples were obtained from a local supermarket for demonstrating the feasibility of the proposal

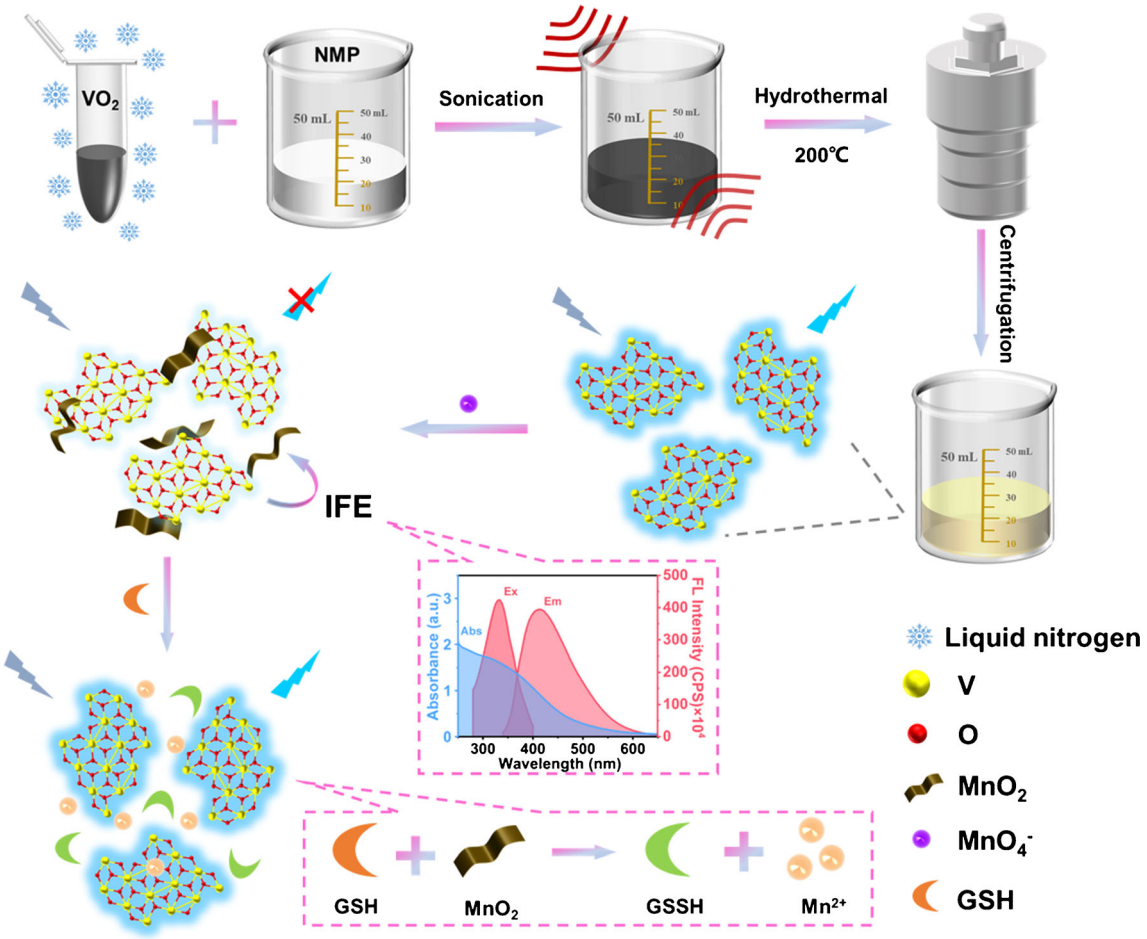

Scheme 1 Schematic illustration of the formation process of bifunctional VO_x QDs by cryogenic-mediated liquid-phase exfoliation and the sensing strategy for GSH

sensor. Firstly, all the samples were washed with ultrapure water and dried in the air, and were ground in a blender. Then the supernatant was obtained by centrifuging and filtering with microporous filters. Treated samples diluted 10^3 times with water were used for further detection.

In an attentional manner, the spiked samples were prepared by adding standard GSH solution into the pristine human serum, fruits, and vegetables. In the monitoring procedure, 100 μL of VO_x QDs solution (10 mg/mL) was added to 900 μL of treated actual sample, and incubated for 3 min at room temperature. Then, the fluorescence spectra were acquired at the excitation wavelength of 330 nm, and the peak wavelength was located at 410 nm.

Results and discussions

Characterization of the prepared VO_x QDs

The excellent optical properties of fluorescent nanoparticles are crucial for the prospects in the application of fluorescent sensors, which impose sets of requirements on the nanoparticles including size, brightness, and quantum yield. In this work, to fabricate smaller quantum dots, we exploited a cryogenic-mediated exfoliation approach to transform VO_2 powder into VO_x QDs with diameters below 15 nm in different solvents. After the liquid-nitrogen treatment, freezing VO_2 bulk and small fissures in the interior were occurred, contributing to the breakage of VO_2 powder into small nanoparticles. Moreover, ultrasonic and solvothermal treatments in three solvents possessing a different surface energy were conducted for further exfoliation. TEM was employed to investigate the morphologies of the three kinds of VO_x QDs, which showed uniform dispersion and well-defined dots with average diameters of 13.15 ± 1.85 nm, 8.06 ± 1.03 nm, and 5.56 ± 0.88 nm ($n = 100$) in DMF, ethanol, and NMP, respectively (Fig. 1A–C). As shown in Fig. 1D–F, all the products exhibited blue emission, and the brightest fluorescence intensity was observed in NMP which may be attributed to the strong polarity and the smallest size. In the inset photos, the quantum dots were colorless using DMF or ethanol as solvent and light yellow using NMP, and, meanwhile, displayed blue

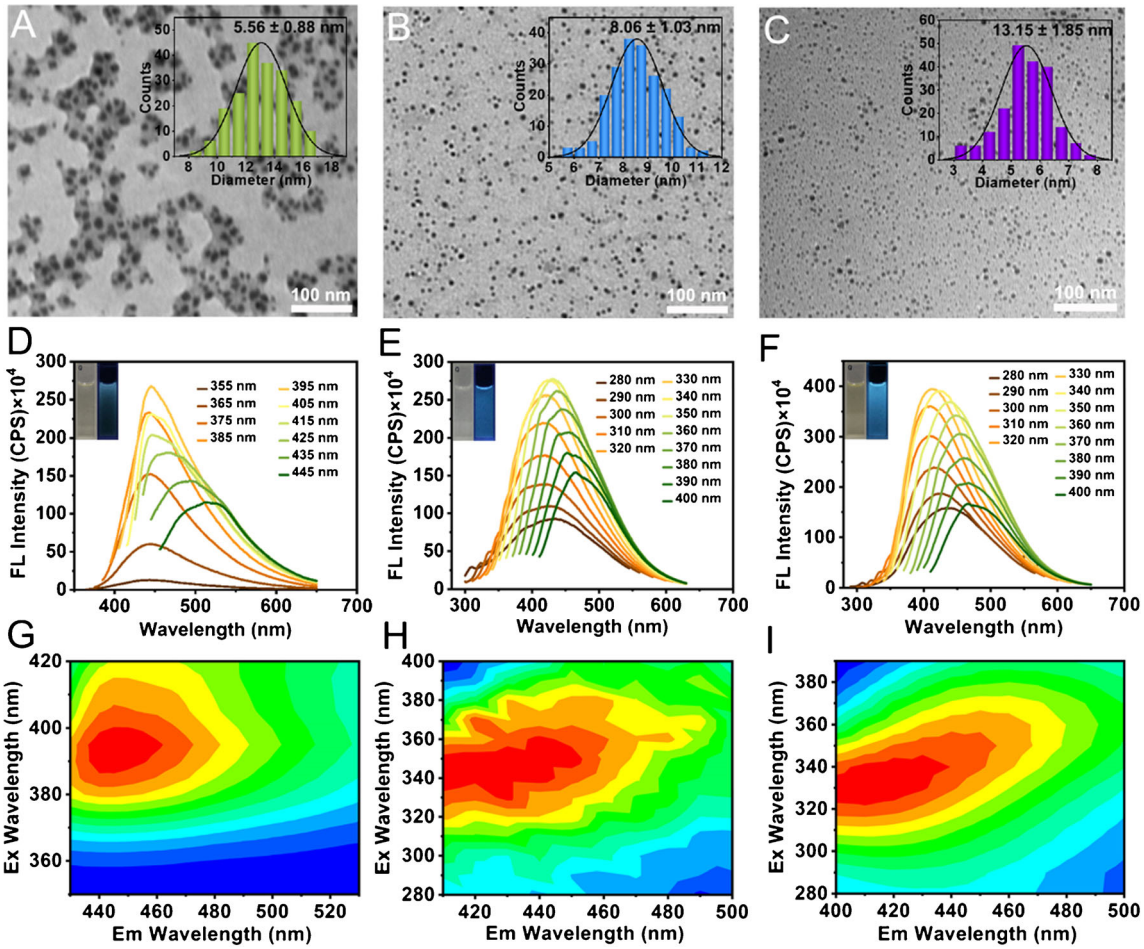

Fig. 1 (**A**–**C**) TEM images and diameter distributions, (**D**–**F**) excitation-dependent fluorescence spectra, (**G**–**I**) excitation-emission-matrix spectra of VO_x QDs prepared in DMF, ethanol, and NMP, respectively

fluorescence in all solvents under 365 nm UV light. The excitation-emission-matrix (EEM) spectra (Fig. 1G–I) further demonstrated the fluorescent characteristic of as-prepared VO_x QDs. Additionally, the quantum yields (QYs) were measured to be 2.5%, 5.3%, and 6.8% for using DMF, ethanol, and NMP, respectively. The varied QYs were probably assigned to the size effects and surface chemistry of the quantum dots caused by different solvents. In addition, the effects of cryogenic-mediated liquid-phase exfoliation and traditional liquid-phase exfoliation methods on VO_x QDs were studied. As shown in Fig. S1, compared with cryogenic-mediated liquid-phase exfoliation, the VO_x QDs via traditional liquid-phase exfoliation showed larger diameters of about 23.30 ± 0.34 nm, lower fluorescence intensity, and smaller QYs of 3.18%. Thus, the above results showed that the performance of cryogenic-mediated liquid-phase exfoliation was better than traditional liquid-phase exfoliation method in the preparation of VO_x QDs. In view of the best fluorescence property, the VO_x QDs prepared in NMP and cryogenic-mediated liquid-phase exfoliation method were selected for next experiment.

The high-resolution transmission electron microscope (HRTEM) image (Fig. 2A) revealed that the synthetic VO_x QDs in NMP were round nanodots and evenly dispersed. The inset exhibited a highly paralleled lattice fringes with interspace of about 0.20 nm, which was consistent with the reported diffraction planes of VO_2 [29]. The VO_x QDs were also characterized by AFM measurement, which further confirmed that the favorable dispersibility and uniformity was similar to that of TEM (Fig. 2B). The atomic force microscopy (AFM) height profiles (inset of Fig. 2B) presented that the typical topographic height of VO_x QDs was about 1.22 ± 0.19 nm, suggesting that the highly exfoliated quantum dots were obtained.

XPS was conducted to identify the surface chemical composition of VO_x QDs. The survey XPS spectrum revealed four main binding energy peaks at 285, 402, 517, and 532 eV corresponding to the elementals of C, N, V, and O (Fig. S2). The high-resolution V 2p spectrum is displayed in Fig. 2C; it was deconvolved into three $2p_{3/2}$-$2p_{1/2}$ spin-orbits doublets. The tiny peaks at 515.1 eV (V $2p_{3/2}$) and 522.8 eV (V $2p_{1/2}$) were attributed to V^{3+}, while the peaks at 516.1 eV (V $2p_{3/2}$)

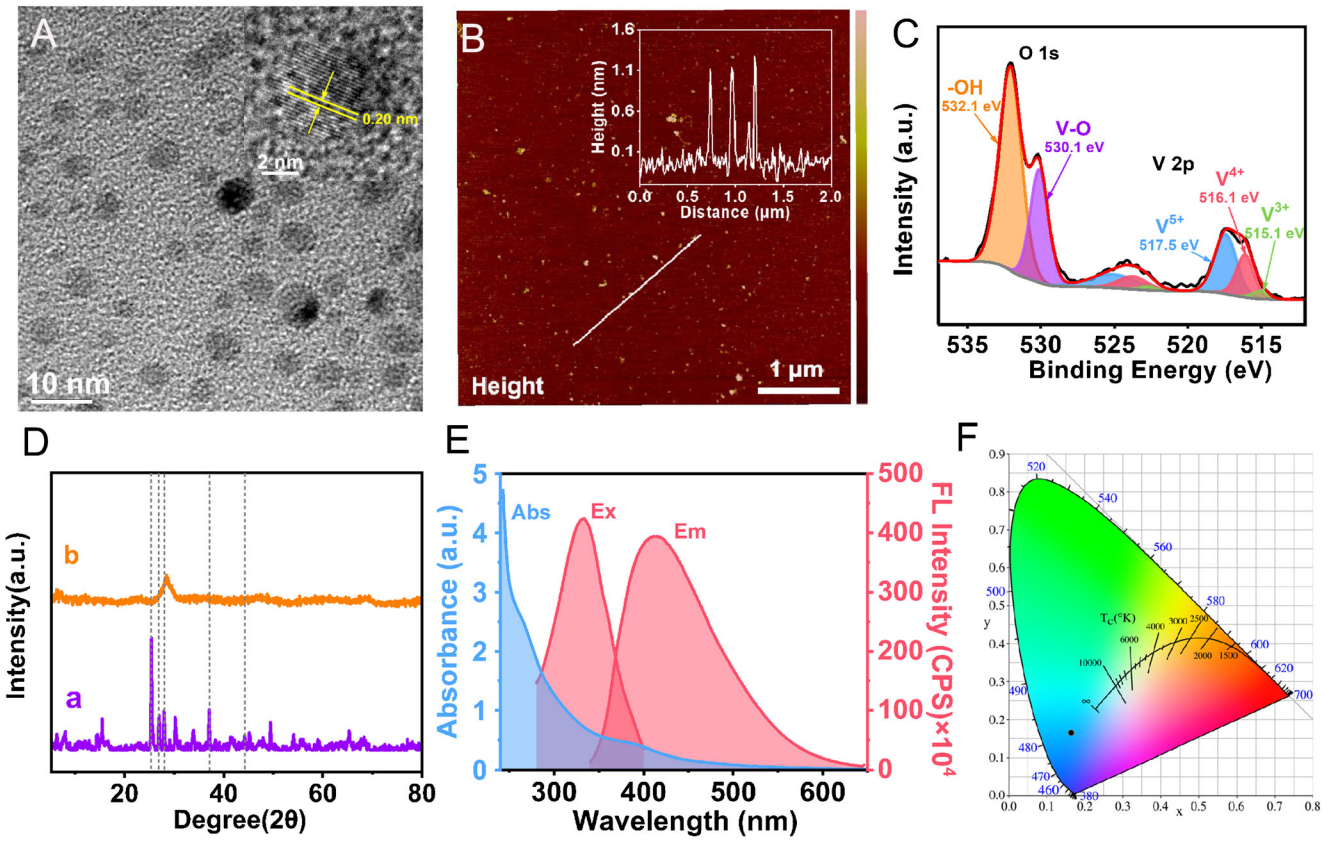

Fig. 2 Characterization for VO_x QDs. **A** HRTEM image (inset: lattice fringes). **B** AFM image (inset: height profile). **C** High-resolution O1s and V2p XPS spectra. **D** XRD patterns. **E** UV-vis absorption, fluorescence excitation, and emission spectra of fluorescent spectra. **F** CIE chromaticity coordinate

and 523.8 eV (V $2p_{1/2}$) were ascribed to V^{4+}. The other V 2p doublet, located at 517.5 eV (V $2p_{3/2}$)/525.2 eV (V $2p_{1/2}$), was derived from V^{5+} [29]. Meanwhile, the contents of V^{3+}, V^{4+}, and V^{5+} were calculated to be 5.7%, 34.5%, and 59.8%. Therefore, the prepared VO_x QDs were coexistent of the multiple valences. In addition, the O 1 s spectrum was fitted by two peaks at 530.1 and 532.1 eV, which were assigned to metal oxide V-O and hydroxyl group -OH [28]. FT-IR reflected the surface functional groups on VO_x QDs (Fig. S3). The band at the region from 3300 to 3500 cm^{-1} was attributed to typical -OH vibration. There was a characteristic peak at 1710 cm^{-1} corresponding to the stretching vibration of carbonyl (C=O), resulting from the solvent molecules NMP. The peak at 1384 cm^{-1} was a typical value for the symmetrical stretching vibration of the carboxyl group. The stretching frequencies of 1026, 840, and 669 cm^{-1} were indicative of V=O, V-O-V, V-O vibrational modes, respectively. Thus, the as-prepared VO_x QDs were consistent with the previous report [29]. As shown in Fig. 2D, XRD was employed to confirm the crystalline structure of the precipitation after centrifugation (a) and synthetic VO_x QDs (b). The distinct peak at $2\theta = 25.5°$ should be indicative of the V_2O_5 (PDF#41-1426), the peaks at 26.9° and 27.9° were attributed to VO_2 (PDF#09-1042), and the ones at 37.1° and 44.3° corresponded to V_2O_3 (PDF#39-0774). By contrast, VO_x QDs exhibited a weaker and broader signal peak on the XRD pattern, which may be associated with the reduced crystallinity and decreased interaction between layers upon the exfoliation process theoretically. Thus, the VO_x QDs were prepared successfully with a highly exfoliated structure.

The optical properties of VO_x QDs were investigated by UV-vis absorption and FL spectra. As presented in Fig. 2E, the characteristic absorption bands of VO_x QDs centered at about 390 nm and the optimal excitation and emission peaks were at 330 and 410 nm. The International Commission on Illumination (CIE) chromaticity diagram further confirmed that VO_x QDs could emit blue fluorescence upon the excitation wavelength at 330 nm (Fig. 2F). The results mentioned above demonstrated the successful preparation of fluorescence VO_x QDs.

VO_x QDs stability

The fluorescent stability of as-prepared VO_x QDs was proved under different ionic strengths, pH values, UV exposure time, and storage time. As shown in Fig. S4A, VO_x QD fluorescence intensity changed insignificantly with the increasing of NaCl concentration from 0 to 100 mM, which confirmed the

salt tolerance of VO_x QDs. Moreover, with the variation of pH from 3 to 11, the fluorescence intensity increased slightly and declined at pH = 10 (Fig. S4B). Thus, the neutral conditions contributed to the emission of VO_x QDs. Additionally, the fluorescence intensity of VO_x QDs fluctuated a little after irradiation at 365 nm UV light for 90 min and storage more than half a month (Fig. S4C and D).

Fluorescence "on-off-on" sensing of GSH

Inspired by the prominent polyvalent and optical characteristics of VO_x QDs, a fluorescent "on-off-on" sensor was designed for GSH determination, where the VO_x QDs served as a bifunctional unit of redox agent and signal indicator. As shown in Fig. 3, VO_x QDs solution emitted conspicuous blue fluorescence with an emission peak at 410 nm (blue curve). After addition of 300 μM MnO_4^-, the fluorescence intensity decreased because of the spontaneous production of MnO_2 nanosheets, and IFE occurred between VO_x QDs and MnO_2 (purple curve). Interestingly, the introduction of GSH which has good reducibility restored the fluorescence of VO_x QDs (red curve) due to the conversion of MnO_2 to Mn^{2+} that cannot induce fluorescence quenching [30]. In view of this phenomenon, VO_x QDs/MnO_4^- offered probability to fabricate an "on-off-on" fluorescence sensing platform for detection of GSH.

Mechanism study of fluorescence quenching and restoration

The synthesized VO_x QDs exhibited strong blue fluorescence. The fluorescence was quenched with MnO_4^- addition, and subsequently recovered by GSH. The possible mechanism

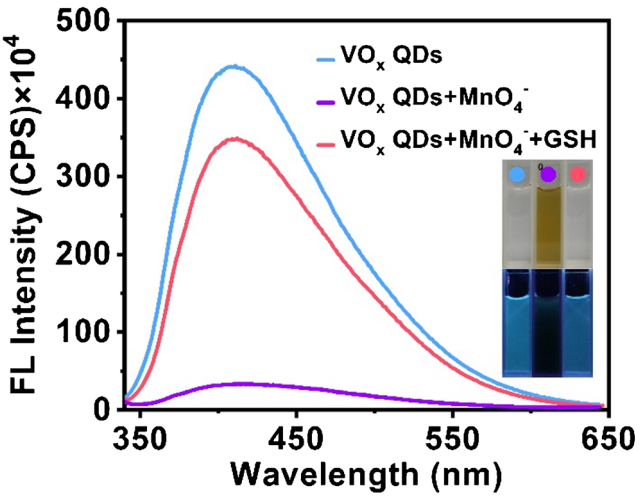

Fig. 3 The different fluorescence spectrum of VO_x QDs in the absence or presence of MnO_4^-, and the recovery spectrum after addition of GSH (excitation: 330 nm). Inset shows the photo representing the corresponding changes under irradiation of 365-nm light

of this "on-off-on" platform for GSH detection was explored by TEM, XPS, UV-vis, and FL spectra.

"Turn-off" From the TEM image (Fig. 4A), it can be observed that the well-defined MnO_2 nanosheets were formed after VO_x QDs reacted with MnO_4^- and VO_x QDs were turned into smaller dimensions with the diameter of 1.74 ± 0.28 nm (n = 100) (Fig. S5A). XPS analysis was employed to investigate the elemental composition. As depicted in Fig. 4C, the two characteristic peaks at 642.1 and 653.6 eV corresponded to Mn $2p_{3/2}$ and Mn $2p_{1/2}$. The Mn 3s peak was analyzed to distinguish Mn oxidation states (Fig. 4D). This peak had two multiplet split components caused by coupling of non-ionized 3s electron with 3d valence-band electrons and magnitude of peak splitting diagnostic of oxidation state. ΔE in the off procedure was 4.7 eV corresponded to the typical value for MnO_2 (Mn^{4+}) [31], indicating that MnO_4^- was spontaneously reduced to MnO_2 by VO_x QDs. Moreover, from the high-resolution V 2p spectrum, the content of V element declined (Fig. S6). Additionally, owing to the overlap between the absorption spectrum of VO_x QDs/MnO_4^- and excitation spectrum of VO_x QDs (Fig. 4E), the fluorescence quenching mechanism could attribute to IFE [32]. Fluorescence lifetime was tested to further study the quenching style and is shown in Fig. 4F. The addition of MnO_4^- caused the fluorescence lifetime of VO_x QDs to change from 9.22 to 7.86 ns, revealing that the fluorescence quenching of VO_x QDs was mainly assigned to the dynamic quenching effect [33].

"Turn-on" Upon the addition of GSH, the MnO_2 nanosheet structure vanished in the TEM image and VO_x QDs still remained in the diameter of 1.79 ± 0.35 nm (n = 100) (Fig. 4B and Fig. S5B). According to the previous reports, the conversion of MnO_2 to Mn^{2+} by GSH may cause the collapse of MnO_2 nanosheets, which contributed to the recovery of fluorescence intensity [27]. In addition, from Fig. 4C, the Mn 2p generated a satellite peak at ~647 eV, which was presented for Mn^{2+}. ΔE in Mn 3s increased to 5.9 eV that coincided with the distance between the two peaks of Mn^{2+} (Fig. 4D), indicating that the MnO_2 has been reduced to Mn^{2+} which cannot cause the fluorescence quenching. From the high-resolution V 2p spectrum (Fig. S6), the content of the V element further reduced, which may be the reason that the fluorescence of VO_x QDs cannot be restored to its original intensity (Fig. 3).

Optimization of experimental conditions

To achieve the superior analytical performance, several essential parameters in "turn-off" and "turn-on" procedure were investigated. The MnO_4^- concentration, solution pH, and reaction time were optimized in the quenching stage. Results revealed that the fluorescence intensity decreased gradually with the incremental MnO_4^- (Fig. S7A), and the quenching rate reached over 90% at

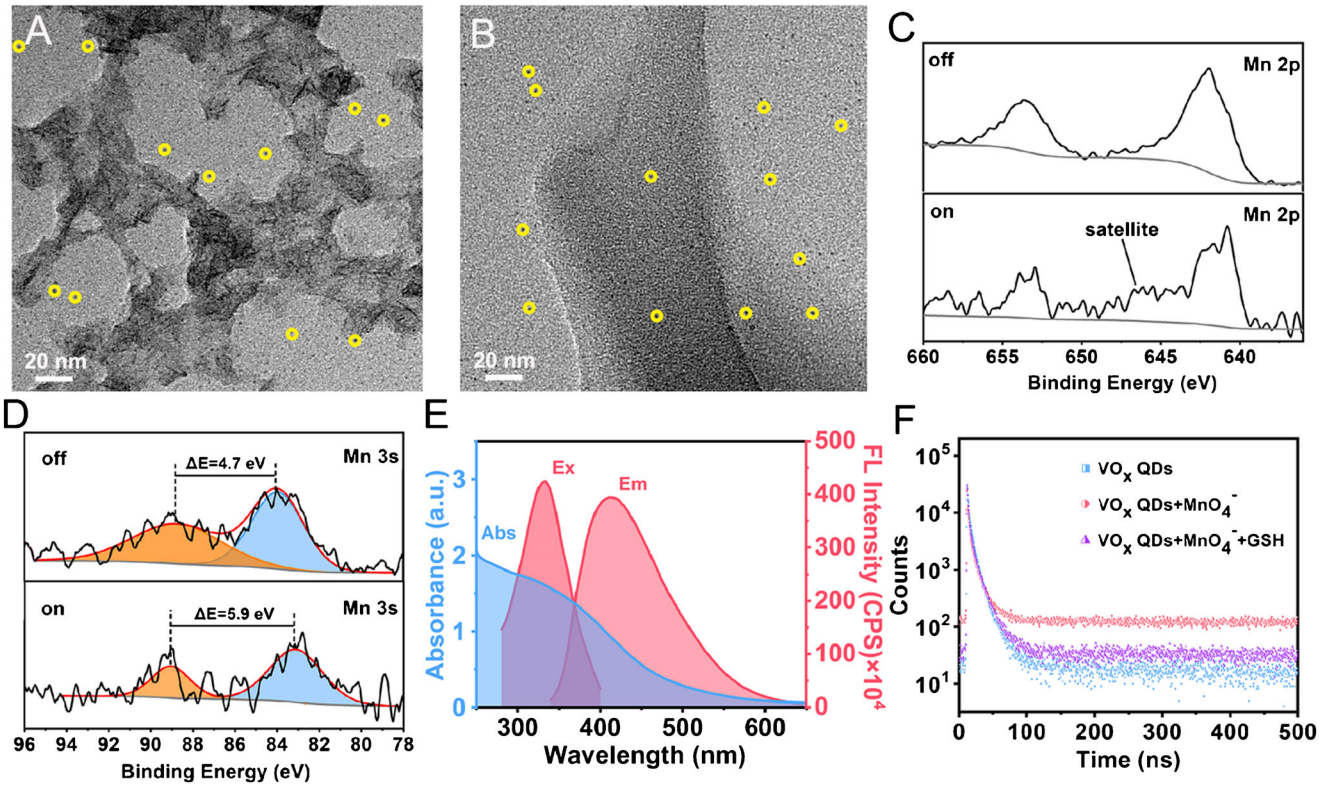

Fig. 4 **A**, **B** TEM images of the spontaneously synthesized MnO_2 nanosheet by VO_x QDs and the decomposed MnO_2 nanosheet by GSH. **C** and **D** were Mn2p and Mn3s XPS spectra in the "turn-off" and "turn-on" procedures. **E** UV-vis absorption of VO_x QDs /MnO_4^-, excitation, and emission spectra of VO_x QDs. **F** Fluorescence lifetime changes of VO_x QDs before and after the reaction with MnO_4^- and GSH

300 μM coupling with an unobvious rise hereafter (the inset of Fig. S7A), where F_0 and F separately represented VO_x QD fluorescence intensity in the absence and presence of MnO_4^- at an emission wavelength of 410 nm. As depicted in Fig. S7B, the maximum quenching rate occurred at pH 7, indicating that the neutral pH could facilitate the redox reaction to form MnO_2 or benefit for the IFE between VO_x QDs and MnO_2. Kinetics was studied to understand the quenching velocity in Fig. S7C; the fluorescence intensity dropped markedly in 100 s and gradually reached equilibrium after 3 min. Similarly, the fluorescence recovered in 4 min after addition of GSH at the restoring phase (Fig. S7D). Therefore, MnO_4^- concentration of 300 μM, solution pH of 7, and reaction time of 3 min were selected for the "turn-off" procedure, and recovery time of 4 min was applied in the "turn-on" procedure.

Detection of GSH

Under the optimal conditions, the "turn-on" strategy was adopted for the quantitative detection of GSH by introducing the VO_x QDs/MnO_4^-. The fluorescence response to different concentrations of GSH was studied through the titration method. As expected, the emission at 410 nm recovered gradually with the increasing GSH (excitation: 330 nm), while it reached an equilibrium after 100 μM (Fig. 5A). The relationship between recovery rate and GSH concentration is shown in Fig. 5B; the values of $(F\text{-}F_q)/F_q$ exhibited an outstanding linear correlation to the GSH, where F_q and F separately represented VO_x QDs/MnO_4^- fluorescence intensity at the emission wavelength of 410 nm in the absence and presence of GSH. The linear range of GSH was 0.5–100 μM with the detection limit of 0.254 μM ($R^2 = 0.998$) (the formula is provided in the Supplementary information). The comparison of the analytical capabilities of this platform with previous reports is listed in Table S1; various fluorescent sensors such as rhodamine-nitronaphthalimide Hg(II) complex; FRET system of N, S-CDs, and Au NPs; and CdSe@SiO2@CdTe fluorescent probe suffered from low anti-interference ability and sophisticated synthetic methods, and required costly material, which largely limited the applications for detecting GSH, indicating that this novel strategy performed with remarkable detection facility and sensitivity for GSH.

Selectivity to target in a complex matrix is a critical index for assessing the fluorescence sensor performance. The fluorescence responses of sensing platform toward other cations (Na^+, Cu^{2+}, Co^{2+}, Ca^{2+}, Cd^{2+}, Zn^{2+}, K^+, Ba^{2+}, Mg^{2+}, Al^{3+}, Fe^{3+}, Hg^{2+}, Mn^{2+}), anions (Cl^-, CO_3^{2-}, NO_3^-, SO_4^{2-}, Ac^-), amino acids (Ser, Ile, Leu, Val, Pro, Gly, Lys, Asp, Met, Glu, L-Glu, Phe, Arg, Thr, His), and molecules (urea, glucose, BSA, AA, Cys) were tested. From Fig. 5C, only GSH and Cys could restore the fluorescence intensity of VO_x QDs,

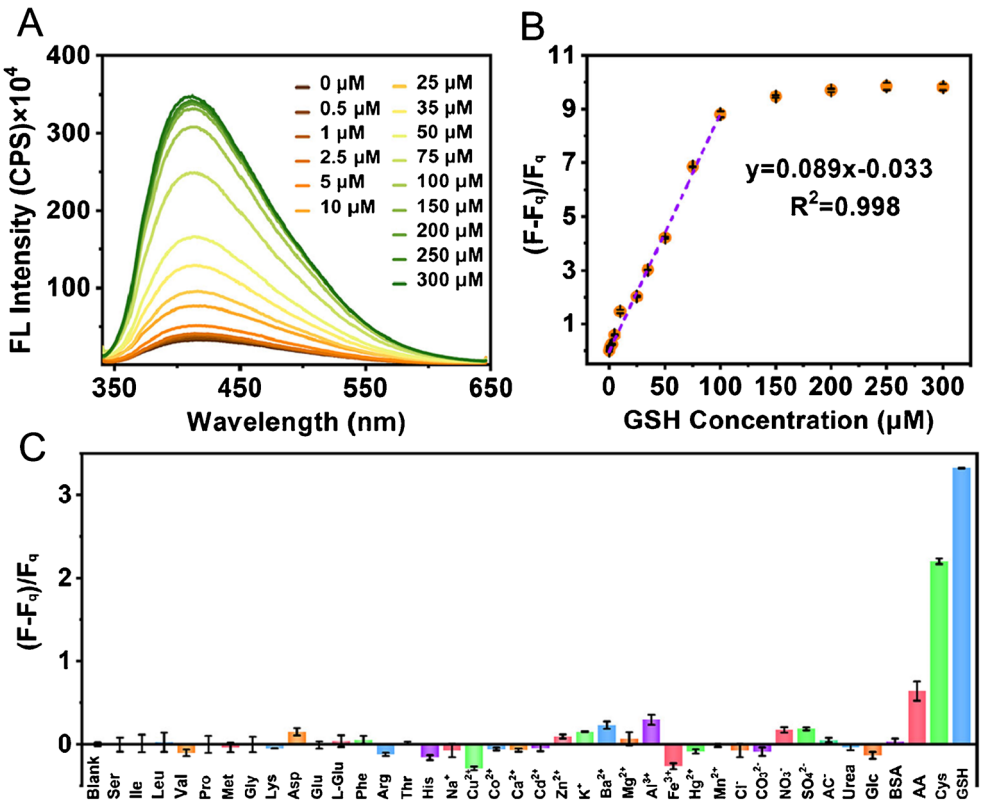

Fig. 5 Emission spectra of VO_x QDs/MnO_4^- system responding to (**A**) GSH with various concentrations (excitation: 330 nm). (**B**) The fitting curve between the recovery rate and the GSH concentrations. (**C**) Selectivity of VO_x QDs/MnO_4^- system for the detection of GSH

while there was no significant difference occurred after adding the other possible interferences. However, the content of Cys in human serum, fruits, and vegetables is low, resulting in a negligible probability of detection interference. Thus, the developed VO_x QDs/MnO_4^- platform was highly specific for GSH recognition.

Quantification of GSH in practical samples

The practical application potential of VO_x QDs/MnO_4^- sensor for GSH detection in human serum, grape, tomato, and cucumber was investigated by spiking a specific concentration of GSH. As the result appeared in Table 1, the GSH contents in human serum, grape, tomato, and cucumber are determined to be 2.13, 7.68, 3.87, and 1.93 μM, respectively. The quantitative percent recovery ranged from 91.96 to 106.87% with the relative standard deviation (RSD) below 5.95%. The acceptable recovery confirmed the feasibility of the proposed sensor for monitoring GSH in different practical samples. In this assay, the samples were diluted 10^3 times during pretreatment to decrease the concentration of each component and achieve the detection range of the sensor. However, the actual

Table 1 Detection of GSH in spiked human serum, fruit, and vegetable samples ($n = 3$)

Sample	Found (μM)	Spiked (μM)	Total found ± RSD (μM)	Recovery (%)	RSD (%)
Human serum	2.13 ± 0.26	5	7.47 ± 0.20	106.87	4.09
		25	25.12 ± 0.19	91.96	0.75
		50	51.89 ± 0.37	99.52	0.74
Purple grape	7.68 ± 0.14	5	12.39 ± 0.09	94.26	1.85
		25	32.17 ± 0.40	94.83	5.95
		50	56.68 ± 0.20	93.94	5.89
Cucumber	3.87 ± 0.06	5	9.03 ± 0.04	103.25	0.79
		25	29.24 ± 0.39	101.47	1.55
		50	54.23 ± 0.69	100.71	1.38
Tomato	1.93 ± 0.05	5	7.09 ± 0.22	103.25	4.31
		25	26.97 ± 0.35	100.18	1.40
		50	51.58 ± 0.44	99.30	0.88

sample matrix is very complicated and contains a variety of reducing species existing in high concentrations, which maybe lead to inaccurate analysis results. Therefore, how to improve the specificity ulteriorly needs to be further explored.

Conclusion

In conclusion, a fluorescence switchable sensor for detection of GSH was constructed by combining VO_x QDs and MnO_4^-.The cryogenic-mediated liquid-phase exfoliation was served as a forceful method to produce bifunctional VO_x QDs with reducibility and blue fluorescence. MnO_4^- can quench their fluorescence which was attributable to the IFE between VO_x QDs and the MnO_2 nanosheets which formed spontaneously through VO_x QDs' reducing effect. Afterward, the redox reaction, which induced the decomposition of MnO_2 nanosheet by GSH, resulted in the fluorescence restoration. Importantly, this platform possessed excellent selectivity and good detection limits for GSH. In addition, the sensor had been successfully used for detecting GSH in human serum, fruits, and vegetables with satisfied recovery. Therefore, the developed sensing strategy provided a favorable mean for monitoring GSH, paving a new way for the application of quantum dots in analytical chemistry. In prospect, for the purpose of improving the accuracy of sensing GSH in an intricate matrix, the absolute specificity toward analyte still needs to be further explored.

Supplementary Information The online version contains supplementary material available at https://doi.org/10.1007/s00604-021-04958-z.

Funding This work was supported by the Talented Program (A279021724) and the Chinese Universities Scientific Fund (No. 2452021123).

Declarations

Conflict of interest The authors declare no competing interests.

References

1. Tan XL, Ji KY, Wang X, Yao R, Han GF, Villamena FA, Zweier JL, Song YG, Rockenbauer A, Liu YP (2020) Discriminative detection of biothiols by electron paramagnetic resonance spectroscopy using a methanethiosulfonate trityl probe. Angew Chem 132: 938–944. https://doi.org/10.1002/anie.201912832
2. Li X, Li S, Liu Q, Cui Z, Chen Z (2019) A triple-channel colorimetric sensor array for identification of biothiols based on color RGB (red/green/blue) as signal readout. ACS Sustain Chem Eng 7:17482–17490. https://doi.org/10.1021/acssuschemeng.9b04740
3. Sharma S, Ghosh SK (2018) Metal-organic framework-based selective sensing of biothiols via chemidosimetric approach in water. ACS Omega 3:254–258. https://doi.org/10.1021/acsomega.7b01891
4. Wu MY, Wang Y, Liu YH, Yu XQ (2018) Dual-site lysosome-targeted fluorescent probe for separate detection of endogenous biothiols and SO_2 in living cells. J Mater Chem B 6:4232–4238. https://doi.org/10.1039/c8tb01152d
5. Liu CL, Liu JP, Zhang WZ, Wang YE, Zhang R (2020a) "Two birds with one stone" ruthenium(ii) complex probe for biothiols discrimination and detection in vitro and in vivo. Adv Sci 7: 2000458. https://doi.org/10.1002/advs.202000458
6. Wang F, Zhou L, Zhao C, Wang R, Fei Q, Luo S, Guo Z, Tian H, Zhu WH (2015) A dual-response BODIPY-based fluorescent probe for the discrimination of glutathione from cystein and homocystein. Chem Sci 6:2584–2589. https://doi.org/10.1039/c5sc00216h
7. Hagen TM, Wierzbicka GT, Sillau AH, Bowman BB, Jones DP (1990) Bioavailability of dietary glutathione: effect on plasma concentration. Am J Phys 259:524–529. https://doi.org/10.1152/ajpgi.1990.259.4.G524
8. Liu C, Cai Y, Wang J, Liu X, Ren H, Yan L, Zhang Y, Yang S, Guo J, Liu A (2020) Facile preparation of homogeneous copper nanoclusters exhibiting excellent tetra-enzyme mimetic activities for colorimetric glutathione sensing and fluorimetric ascorbic acid sensing. ACS Appl Mater Interfaces 12:42521–42530. https://doi.org/10.1021/acsami.0c11983
9. Yang Q, Li J, Wang X, Xiong H, Chen L (2019) Ternary emission of a blue-, green-, and red-based molecular imprinting fluorescence sensor for the multiplexed and visual detection of bovine hemoglobin. Anal Chem 91:6561–6568. https://doi.org/10.1021/acs.analchem.9b00082
10. Song Y, Zhu CZ, Song JH, Li H, Du D, Lin YH (2017) Drug-derived bright and color-tunable n-doped carbon dots for cell imaging and sensitive detection of Fe^{3+} in living cells. ACS Appl Mater Interfaces 9:7399–7405. https://doi.org/10.1021/acsami.6b13954
11. Wilcoxon JP, Samara GA, Provencio PN (1999) Optical and electronic properties of Si nanoclusters synthesized in inverse micelles. Phys B 60:2704–2714. https://doi.org/10.1103/PhysRevB.60.2704
12. Gopalakrishnan D, Damien D, Li B, Gullappalli H, Pillai VK, Ajayan PM, Shaijumon MM (2015) Electrochemical synthesis of luminescent MoS_2 quantum dots. Chem Commun 51:6293–6296. https://doi.org/10.1039/c4cc09826a
13. Mathew S, Gopinadhan K, Chan T, Yu X, Zhan D, Cao L, Rusydi MA, Breese BH, Dhar S, Shen ZX (2012) Magnetism in MoS_2 induced by proton irradiation. Appl Phys Lett 101:102103. https://doi.org/10.1063/1.4750237
14. Michalet X, Pinaud FF, Bentolila LA, Tsay JM, Doose S, Li JJ, Sundaresan G, Wu AM, Gambhir SS, Weiss S (2005) Quantum dots for live cells, in vivo imaging, and diagnostics. Science 307: 538–544. https://doi.org/10.1126/science.1104274
15. Kang S, Kim Y, Jang E, Kang Y, Han S (2020) Fundamental limit of the emission linewidths of quantum dots: an ab initio study on CdSe nanocrystals. ACS Appl Mater Interfaces 12:22012–22018. https://doi.org/10.1021/acsami.0c02904
16. Chen S, Jiang H, Cheng Q, Wang G, Petr S, Li C (2021) Amorphous vanadium oxides with metallic character for asymmetric supercapacitors. Chem Eng J 403:126380. https://doi.org/10.1016/j.cej.2020.126380
17. Qi Y, Xu Q, Tu G, Fu Y, Zhu W (2020) Vanadium oxides anchored on nitrogen-incorporated carbon: an efficient heterogeneous catalyst for the selective oxidation of sulfide to sulfoxide. Catal Commun 145:106101. https://doi.org/10.1016/j.catcom.2020.106101
18. Fernando JFS, Siriwardena DP, Firestein KL, Zhang C, Treifeldt JEV, Lewis CEM, Wang T, Dubal DP, Golberg DV (2020) Enriched pseudocapacitive lithium storage in electrochemically

activated carbonaceous vanadium(IV, V) oxide hydrate. J Mater Chem A 8:13183–13196. https://doi.org/10.1039/d0ta04191b
19. Zhang C, Xu Y, Lu P, Wei C, Zhu C, Yao H, Xu F, Shi J (2019) Cryogenic exfoliation of non-layered magnesium into two-dimensional crystals. Angew Chem 131:8906–8910. https://doi.org/10.1002/anie.201903485
20. Wang Y, Liu Y, Zhang J, Wu J, Xu H, Wen X, Zhang X, Tiwary CS, Yang W, Vajtai R (2017) Cryo-mediated exfoliation and fracturing of layered materials into 2D quantum dots. Sci Adv 3: e1701500. https://doi.org/10.1126/sciadv.1701500
21. Daniele M, Gianfranco U, Giovanni V (2018) Nanomorphological investigation of graphite surface after cryo-ultrasonication in liquid nitrogen by atomic force microscopy. Micro Nano Lett 13:546–551. https://doi.org/10.1049/mnl.2017.0682
22. Luo X, Zhang W, Han Y, Chen X, Zhu L, Tang W, Wang J, Yue T, Li Z (2018) N,S co-doped carbon dots based fluorescent "on-off-on" sensor for determination of ascorbic acid in common fruits. Food Chem 258:214–221. https://doi.org/10.1016/j.foodchem.2018.03.032
23. Yang Q, Wang X, Peng H, Arabi M, Chen L (2020) Ratiometric fluorescence and colorimetry dual-mode assay based on manganese dioxide nanosheets for visual detection of alkaline phosphatase activity. Sensors Actuators B Chem 302:127176. https://doi.org/10.1016/j.snb.2019.127176
24. Yang Q, Li C, Li J, Arabi M, Wang X, Peng H, Xiong H, Choo J, Chen L (2020) Multi-emitting fluorescence sensor of MnO_2-OPD-QD for the multiplex and visual detection of ascorbic acid and alkaline phosphatase. J Mater Chem C 8:5554–5561. https://doi.org/10.1039/c9tc07072a
25. Xue HY, Yu M, He KY, Liu YN, Wang L (2020) A novel colorimetric and fluorometric probe for biothiols based on MnO_2 NFs-rhodamine B system. Anal Chim Acta 1127:39–48. https://doi.org/10.1016/j.aca.2020.06.039
26. Sohal N, Maity B, Basu S (2020) Carbon dot-MnO_2 nanosphere composite sensors for selective detection of glutathione. ACS Appl Nano Mater 3:5955–5964. https://doi.org/10.1021/acsanm.0c01088
27. Deng R, Xie X, Vendrell M, Chang YT, Liu X (2011) Intracellular glutathione detection using MnO(2)-nanosheet-modified upconversion nanoparticles. J Am Chem Soc 133:20168–20171. https://doi.org/10.1021/ja2100774
28. Huang L, Niu Y, Li R, Liu H, Wang Y, Xu G, Li Y, Xu Y (2019) VO_x quantum dots with multienzyme-mimic activities and the application in constructing a three-dimensional (3D) coordinate system for accurate discrimination of the hydrogen peroxide over a broad concentration range. Anal Chem 91:5753–5761. https://doi.org/10.1021/acs.analchem.8b05923
29. Huang L, Niu Y, Xu G, Wang Y, Yuan L, Xu Y, Li R (2018) Generation of vanadium oxide quantum dots with distinct fluorescence and antibacterial activity via a room-temperature agitation strategy. ChemNanoMa 4:1048–1053. https://doi.org/10.1002/cnma.201800257
30. Sun JL, Liu F, Yu WQ, Jiang QY, Hu JL, Liu YH, Wang F, Liu XQ (2019) Highly sensitive glutathione assay and intracellular imaging with functionalized semiconductor quantum dots. Nanoscale 11: 5014–5020. https://doi.org/10.1039/c8nr09801h
31. Wang Y, Cai L, Wang Q, Zhao M, Li J (2019) Spontaneous reduction of $KMnO_4$ with MoS_2 quantum dots for glutathione sensing in tumor. Analyst 145:836–843. https://doi.org/10.1039/c9an02239b
32. Jia P, Bu T, Sun XY, Liu YN, Liu JH, Wang QZ, Shui YH, Guo SW, Wang L (2019) A sensitive and selective approach for detection of tetracyclines using fluorescent molybdenum disulfide nanoplates. Food Chem 297:124969. https://doi.org/10.1016/j.foodchem.2019.124969
33. Chao P, Xing HH, Fan XS, Xue Y, Li J, Wang EK (2019) Glutathione regulated inner filter effect of MnO_2 nanosheets on boron nitride quantum dots for sensitive assay. Anal Chem 91: 5762–5767. https://doi.org/10.1021/acs.analchem.8b05961